JGR Atmospheres

RESEARCH ARTICLE
10.1029/2022JD036940

# Regional Perspective of Hadley Circulation and Its Uncertainties Among Different Datasets: Spread in Reanalysis Datasets

**Yadi Li[1,2], Xichen Li[1], Shang-Ping Xie[3], Gan Zhang[4], Zhuo Wang[5], Wenzhu Wang[1,2], and Yurong Hou[1,2]**

[1]International Center for Climate and Environment Sciences (ICCES), Institute of Atmospheric Physics, Chinese Academy of Sciences, Beijing, China, [2]University of Chinese Academy of Sciences, Beijing, China, [3]Scripps Institution of Oceanography, University of California San Diego, La Jolla, CA, USA, [4]Atmospheric and Oceanic Sciences Program, Princeton University, Princeton, NJ, USA, [5]Department of Atmospheric Sciences, University of Illinois at Urbana-Champaign, Urbana, IL, USA

**Key Points:**

- The three-dimensional structure of Hadley circulation (HC) are examined based on eight state-of-the-art reanalysis datasets
- Different reanalysis datasets share similar spatial structure of the regional Hadley cells but with different amplitudes
- The trends of the regional HC show a clear spread in spatial structure and amplitudes among different reanalyses

**Correspondence to:**
X. Li and S.-P. Xie,
lixichen@mail.iap.ac.cn;
sxie@ucsd.edu

**Citation:**
Li, Y., Li, X., Xie, S.-P., Zhang, G., Wang, Z., Wang, W., & Hou, Y. (2022). Regional perspective of Hadley circulation and its uncertainties among different datasets: Spread in reanalysis datasets. *Journal of Geophysical Research: Atmospheres*, *127*, e2022JD036940. https://doi.org/10.1029/2022JD036940

Received 5 MAY 2022
Accepted 24 NOV 2022

**Abstract** The Hadley circulation (HC) is often considered zonally uniform and defined using the zonally averaged mass stream function (MSF). However, the longitudinal distribution of the overturning circulation is far from uniform, which has profound impacts on regional climates. This study uses a recently developed technique to examine the three-dimensional MSF and thus the regional manifestations of the HC, and evaluates their climatology and seasonality in eight commonly used reanalysis datasets. This comparison emphasizes the spatial structure and the intensity of four regional Hadley cells, defined based on the natural boundaries of the three-dimensional MSF. Specifically, two Hadley cells are located in the Indo-Pacific warm pool region, with a strong and relatively deep cell extending from the equator to mid-latitudes in each hemisphere. The other two cells are located over the East Pacific-Atlantic sector, which is relatively weak and shallow, confined within the tropics and subtropics. The spatial structure of each regional cell is nearly identical among all reanalysis datasets, with pairwise spatial correlation coefficients higher than 0.9. However, the intensities of regional MSF show a large spread among these datasets. The range of this spread reaches up to about half of the means of all reanalysis datasets over the Indo-Pacific warm pool region in the Northern Hemisphere. Further analysis reveals a large spread in the spatial structure and the amplitudes of the regional HC trends among different reanalyses. The findings highlight uncertainties in the regional circulation of modern reanalysis datasets and have implications for interpreting past and future circulation changes.

## 1. Introduction

The Hadley Circulation (HC), usually defined using the global zonal mean meridional mass stream function (MSF; Bjerknes, 1966; Hadley, 1735), is the main feature of the large-scale atmospheric circulation over the tropical and sub-tropical regions (Held & Hou, 1980). It plays a key role in transporting energy and moisture across different latitudes (Diaz & Bradley, 2004; Hou, 1998), not only between the tropics and higher latitudes, but also between the Northern and Southern Hemispheres (NH and SH; Hou, 1998; Lindzen, 1994). The warm and moist air mass rises in the tropics, especially over the Indo-Pacific warm pool (IPWP) and the intertropical convergence zone (ITCZ), and sinks in the higher latitudes in both hemispheres (Hadley, 1735; Held & Hou, 1980). The HC shows a strong seasonality, with the strongest and largest circulation usually appearing over the winter hemisphere, together with a cross-equatorial energy transport from the summer hemisphere to the winter one (Lindzen & Hou, 1988; Oort & Rasmusson, 1970). In spring and autumn, the HC is quasi-symmetric about the equator (Dima & Wallace, 2003; Oort & Yienger, 1996). The strength and expansion of HC are tightly associated with the meridional gradient of sea surface temperature (SST; Oort & Yienger, 1996; Quan et al., 2004) and the baroclinic instability over the sub-tropics and mid-latitudes (Held, 2001; Lindzen, 1994).

Recent studies have revealed a long-term trend in the HC expansion and intensity, in response to the increased anthropogenic greenhouse gas concentration (Allen et al., 2014; Amaya et al., 2017; Staten et al., 2018; Tao et al., 2015) and the long-term variabilities of the ocean surface temperature (Kim et al., 2017; Lu et al., 2009; Waugh et al., 2015). In particular, the edges of the HC showed a poleward shift in both hemispheres, supported by recent observations (Fu et al., 2006; Hu & Fu, 2007) and numerical model simulations (Frierson et al., 2007; Johanson & Fu, 2009; Lu et al., 2007), although the trend has a large spread among different datasets, ranging from 0.25° to 3° latitude per decade (Davis & Rosenlof, 2012; Fu & Lin, 2011; Hu & Fu, 2007; Nguyen

et al., 2015; Staten et al., 2018). The intensity and the width of the HC are tightly associated with tropical ocean variabilities. For example, El Niño events may strengthen the HC and compress its width (Lu et al., 2008; Quan et al., 2004; Seager et al., 2003). The Northern and Southern Annular Modes (NAM and SAM), as well as the Atlantic Multidecadal Oscillation, may also modulate the intensity and the location of the HC (Feng et al., 2017; Guo, Li, & Feng, 2016; Previdi & Liepert, 2007; Zheng et al., 2015).

The trends of the HC also show strong regional variations (Chen et al., 2014; Freitas et al., 2016; Kim et al., 2017; Studholme & Gulev, 2018). A series of studies thus attempted to decompose the global HC into regional cells, and further evaluate its intensity and expansion in a regional perspective (Grise et al., 2018; Nguyen et al., 2017; Staten et al., 2019). Recently, a local meridional MSF, similar to the global ones but with a longitudinal distribution, has been constructed based on the irrotational flow of the atmospheric circulation (Cheng et al., 2020; Feng et al., 2018; Huang et al., 2018, 2019; Nguyen et al., 2017; Staten et al., 2019; Sun et al., 2018; Zhang & Wang, 2013, 2015). It has now been frequently used to represent the regional Hadley cells and clearly illustrates the three-dimensional structure of the circulation, as well as its meridional transport of the air mass and energy (Nguyen et al., 2017; Staten et al., 2019).

It is difficult to identify the HC directly based on the observations. We usually integrate the meridional wind velocity in the reanalysis datasets to represent the HC. The reanalysis is considered as a proxy of the real world in this metric, leaving it a fundamental issue to evaluate the quality of these reanalysis datasets in representing the intensity and structure of the HC. Stachnik and Schumacher (2011) compared the HC among eight reanalysis datasets in a global perspective, revealing a large spread in the HC intensity between these datasets. Mathew et al. (2016) indicated that the weaker MSF in NCEP is primarily due to its lower vertical resolution. In addition, Feng et al. (2016) revealed a spread in the width, the equatorward edge, and the poleward edges of the HC among different reanalysis datasets. However, previous studies usually evaluated the spread of the reanalysis datasets in a global zonal-mean perspective and did not provide a clear picture of the regional HC. It is thus important to evaluate the consistency of reanalysis datasets in representing the intensity and structure of the HC in a regional perspective.

In this study, we first examine the climatological characteristics of the HC in a regional perspective. Meanwhile, we evaluate the spread of the HC among eight reanalysis datasets, and further quantify the difference among each dataset. In Section 2, we introduce the datasets and the statistical methods used in this work. We then integrate a three-dimensional meridional MSF all over the globe in each reanalysis dataset, based on the irrotational flow of the atmosphere in Section 3, and decompose the global HC into four Hadley cells, following the horizontal boundaries of these clockwise and anti-clockwise circulations. In Section 4, we evaluate the spread of the climatological features and the trends of the regional HC among different reanalyses, focusing on the spatial structure of these Hadley cells. Finally, a summary and discussion are presented in Section 5.

## 2. Data and Method

The monthly mean horizontal wind and precipitation data from eight reanalysis datasets are employed in this study: (a) the Twentieth Century Reanalysis (20CR; Compo et al., 2011); (b) the Climate Forecast System Reanalysis (CFSR; Saha et al., 2010); (c) the Interim reanalysis data from the European Center for Medium-Range Weather Forecasts (ERA-Interim (ERAI); Dee et al., 2011); (d) the ECMWF Reanalysis version 5 (ERA5; Hersbach et al., 2020); (e) the Japanese 55 yr Reanalysis (JRA55; Kobayashi et al., 2015); (f) the Modern-Era Retrospective analysis for Research and Applications (MERRA; Rienecker et al., 2011); (g) the MERRA version-2 (MERRA2; Gelaro et al., 2017); and (h) the NCEP-DOE Reanalysis version-2 (NCEP2; Kanamitsu et al., 2002). All eight reanalysis datasets are first interpolated into a common horizontal ($2° \times 2°$) and vertical coordinate (20 levels). Detailed information of the reanalysis datasets is summarized in Table 1. The ensemble mean of the eight reanalysis datasets is calculated to depict the common features of the regional HC and to serve as a reference when examining the spread among different datasets. We also used the monthly mean SST dataset from the Extended Reconstructed SST version 5 (ERSST v5; Huang et al., 2017).

The HC is usually defined as the meridional-vertical MSF all around the globe, as shown in Figure 1 (Oort & Yienger, 1996), in which the periodical boundary condition (longitudinal) cancels the zonal mass flux, leaving the

**Table 1**
*Detailed Information of the Eight Reanalysis Datasets Used in This Study*

| Name | Organization | Assimilation method | Satellite data processing | Spatial resolution | Vertical layer | Temporal resolution | Model grid resolution |
|---|---|---|---|---|---|---|---|
| 20CR | NOAA-CIRES | 3D-VAR | — | 2° × 2° | 24 levels | January 1979 to December 2012 | T62 |
| CFSR | NCEP | 3D-VAR | Radiances | 2.5° × 2.5° | 37 levels | January 1979 to December 2019 | T382 |
| ERAI | ECMWF | 4D-VAR | Radiances | 2.5° × 2.5° | 37 levels | January 1979 to December 2018 | T225 |
| ERA5 | ECMWF | 4D-VAR | Radiances | 0.25° × 0.25° | 37 levels | January 1979 to December 2019 | T639 |
| JRA55 | JMA | 4D-VAR | Radiances | 1.25° × 1.25° | 37 levels | January 1979 to December 2019 | T319 |
| MERRA | NASA | 3D-VAR | Retrievals | 2/3°× 1/2° | 42 levels | January 1979 to December 2015 | — |
| MERRA2 | NASA | 3D-FGAT | Retrievals | 0.5° × 0.625° | 42 levels | January 1980 to December 2019 | — |
| NCEP2 | NCEP-NCAR | 3D-VAR | Retrievals | 2.5° × 2.5° | 17 levels | January 1979 to December 2019 | T62 |

meridional and vertical velocity a non-divergent flow. The global MSF is obtained by integrating the zonal-mean meridional velocity from the top of the atmosphere to the surface, in pressure coordinate:

$$\psi(y,p) = \frac{2\pi R}{g}\int [\overline{v}]\cos\phi dp, \tag{1}$$

where $\psi(y,p)$ is the global zonal-mean MSF, $R$ is the radius of the earth, $\overline{v}$ is the temporal average meridional wind, $\phi$ is latitude and the bracket represents the zonal average all around the globe. This MSF represents the mass transport in the upper and lower atmosphere in a global perspective.

Several recent studies constructed the regional MSF of the HC (Cheng et al., 2020; Feng et al., 2018; Huang et al., 2018, 2019; Nguyen et al., 2017; Staten et al., 2019; Sun et al., 2018; Zhang & Wang, 2013). In these studies, the horizontal velocity at each pressure level is decomposed into irrotational and nondivergent flows. Given that only the irrotational flow contributes to vertical motion, the vertical velocity associated with the meridional circulation may be regarded as part of the HC:

$$\frac{\partial v_\chi}{\partial y} + \frac{\partial \omega_H}{\partial p} = 0, \tag{2}$$

where the $v_\chi$ represents the irrotational meridional flow, the $\omega_H$ represents the vertical velocity component associated with the regional HC. The regional HC is then calculated through vertical integration of the irrotational velocity within a given longitude range:

$$\psi(x,y,p) = \frac{R}{g}\int [\overline{v_\chi}]\cos\phi dp \tag{3}$$

where the $\psi(x,y,p)$ represents the local MSF, and the bracket represents the zonal average over a given longitude range. A detailed calculation of the regional MSF can be found in Zhang and Wang (2013, 2015). The method allows us to evaluate the regional variations of the HC.

Based on this method, we first calculate the meridional-vertical MSF of the HC at each longitude and obtain a three-dimensional distribution of the HC all over the globe. We further illustrate the horizontal distribution of the HC in Figures 2a and 2b. The color map in Figure 2a shows the maximum strength (along vertical direction) of the regional MSF of the HC at each grid point, while the pressure level at which the HC achieves the maximum (minimum) value is illustrated in Figure 2b, which shows that the largest mass transportation at this grid point appears above and below this level.

With a horizontal distribution of the regional MSF (Figures 2a and 2b), we further examine the HC in a regional perspective. The global HC may be first

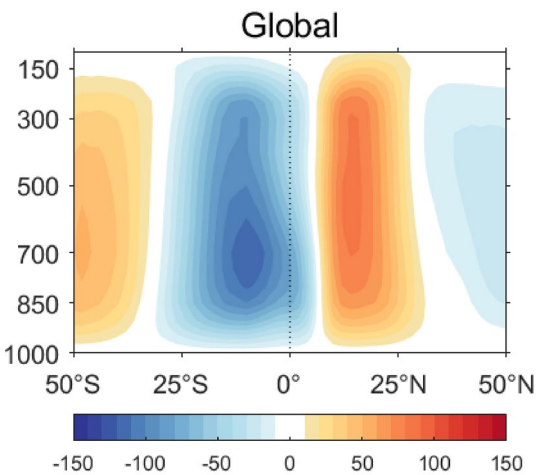


**Figure 1.** The annual mean climatology of the global zonal-mean mass stream function (MSF; $10^9$ kg $s^{-1}$) based on the ensemble-mean of the eight reanalysis datasets. The positive (negative) values indicate clockwise (anti-clockwise) flows.

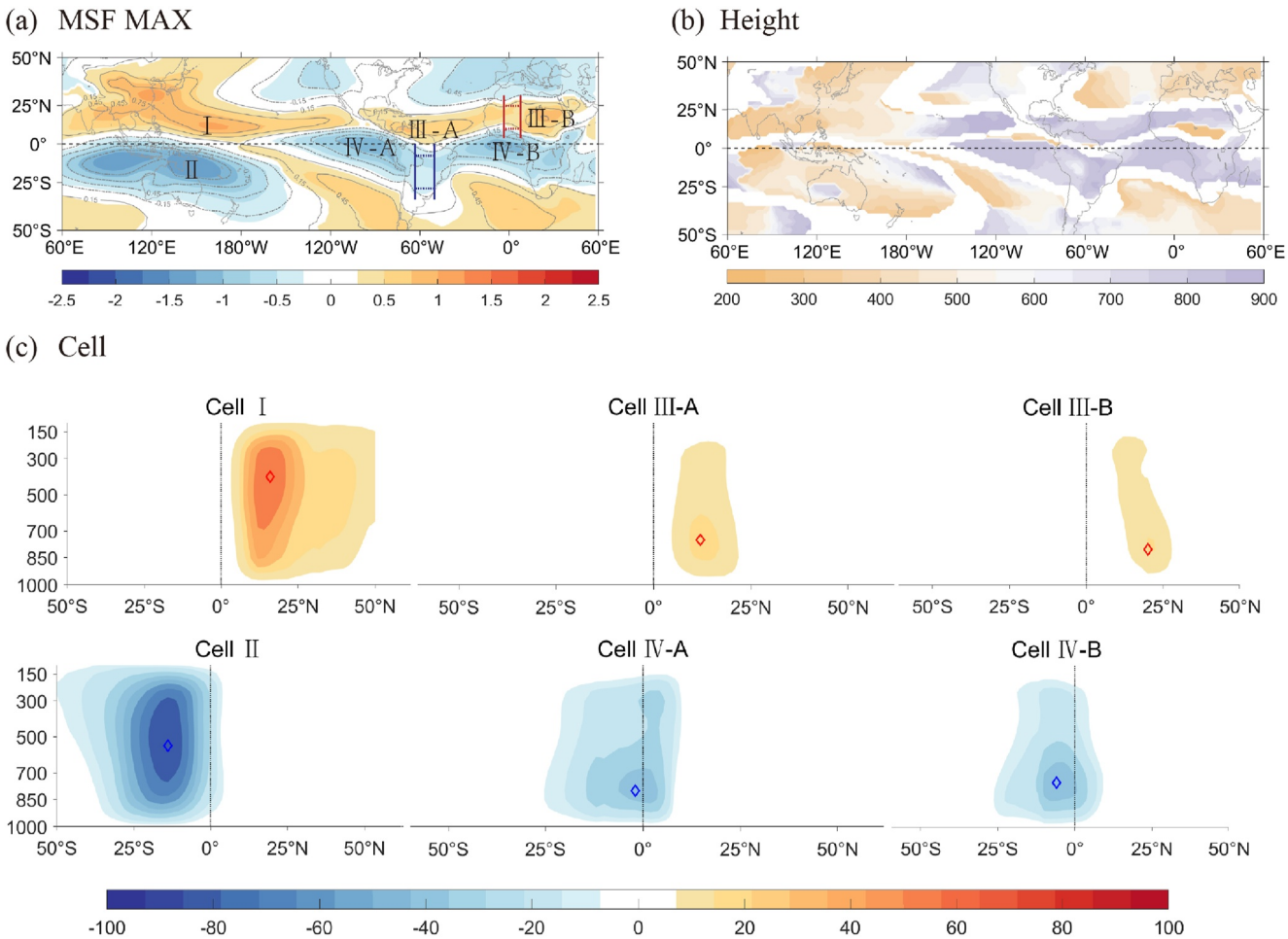


**Figure 2.** The horizontal and vertical spatial distribution of the regional mass stream function (MSF) based on the ensemble-mean of the eight reanalysis datasets in annual mean. (a) The horizontal distribution of the strength of the ensemble-mean meridional MSF (shading, unit is $10^9$ kg $s^{-1}$) with gray contours representing the MSF values first reach 10%, 30%, 50%, and 70% of the peak value. The red and the blue lines represent the areas within which Cell III (red lines) and Cell IV (blue lines) are divided into Cell III-A, III-B and Cell IV-A, IV-B, based on the minimum value of the MSF within these two areas. (b) The horizontal distribution of the height (shading, unit is hPa) of the strength which is greater than 10% threshold. (c) The vertical distribution of the zonal integrated regional circulation of each Hadley cell (shading, unit is $10^9$ kg $s^{-1}$) with rhombus representing the circulation center.

divided into four sectors naturally (Figure 2a), bounded by the reverse of the positive and negative values of the MSF, hereafter referred to as the Hadley Cells I–IV. Within each of these four cells, the regional MSF is always positive (or negative), thus avoiding the cancellation of the mass transport within one cell when zonally integrating the MSF. One pair of the cells appear over the IPWP region, from 60°E to about 120°W, hereafter defined as Cell I (NH) and Cell II (SH) for the components in the Northern and Southern Hemispheres (Figure 2a), respectively. This pair of cells is relatively stronger (Figures 2a and 2c) and wider-extended compare with the other regional Hadley cells, and is on a relatively higher level (Figure 2b), in that they are driven by the strong deep atmospheric convection over the IPWP region. The other pairs appear over the Eastern Pacific-Atlantic Oceans, also covering the tropical Africa and America, hereafter defined as the Cell III (NH) and Cell IV (SH). These two cells are relatively weaker (Figures 2a and 2c) and thinner, on a lower level of about 700 hPa (Figure 2b), considering that the climatological SST over the equatorial Eastern Pacific and the Tropical Atlantic is relatively lower than that over the IPWP region, leading to a comparatively weaker and shallower deep-convection over these areas (Lau et al., 1997; Zhang, 1993). The latter two cells cover the tropical and subtropical regions over the Eastern Pacific and the Tropical Atlantic, and are dominated by two circulation centers, one covering the Eastern Pacific, and the other covering the Tropical Atlantic. We thus further divide Cell III and IV each into two sub-cells (III-A, III-B, IV-A, and IV-B) based on their geological distribution, where A and B represent the western (the Pacific) and eastern (the Atlantic) sectors, respectively.

We use the empirical orthogonal function (EOF) analysis to retrieve the main features of these three-dimensional MSF of the regional HC. In addition, the spatial pattern correlation is calculated to investigate the coherency and spread among different reanalysis data sets. Linear regression method is used to investigate the relationship between the regional HC and tropical precipitation. Student's *t* test is used to calculate the statistical significance of the spatial correlation and linear regression.

## 3. Hadley Cells in Reanalysis Datasets

We first illustrate the climatological states of the annual mean MSF based on the ensemble-mean of the eight reanalysis datasets (Figure 2). Figure 2a shows the horizontal distribution of the strength of the MSF over the global tropical and sub-tropical regions, Figure 2b illustrates the pressure level where the MSF reaches its maximum (minimum) value at each grid point. We then integrate each cell along the zonal direction and evaluate the total mass transport (magnitude) and the vertical structure of these cells, as shown in Figure 2c. For example, the vertical structure of Cell I in Figure 2c represents the zonal integration of the three-dimensional MSF within the domain of Cell I in Figure 2a (spanning the area between 60°E and 120°W), whose regional MSF is always positive (see Figure 2a).

The regional MSF of the HC is characterized by a strong zonal variation, with the strongest and the most extensive cells (Cell I and II) over the IPWP region, extending from the equator to 50°N and 40°S, respectively (Figure 2a). These two strong cells are tightly associated with the Asian and Australian monsoon systems (Feng et al., 2018; Sun et al., 2018), involving an intense atmosphere-land-ocean interaction and having broad implications on the structure, amplitude, and seasonality of regional circulations (Dima & Wallace, 2003; Sun & Zhou, 2014). The cells (Cell III and IV) over the Eastern Pacific and the Atlantic Ocean are weaker and are constrained within 25° from the equator over each hemisphere. These two cells are associated with the American monsoon system (Kamae et al., 2017; Vera et al., 2006) and the African monsoon (Rossignolstrick, 1983; Trenberth et al., 2000). In addition, the vertical structure of the IPWP cells (Cell I and II) and the East Pacific-Atlantic cells (Cell III and IV) also show distinct features. As shown in Figures 2b and 2c, Cells I and II both reach their maximum (minimum) MSF value at about 500 hPa, while the largest MSF value of Cell III and IV appears below 700 hPa, illustrating a deeper overturning circulation over the IPWP region than that over the Eastern Pacific–Atlantic Oceans (Zhang et al., 2008).

We further integrate Cells I, II, III-A/B, and IV-A/B respectively to examine the vertical structure of the regional Hadley cells and to quantify the amplitude of each cell (Figure 2c). In the NH, Cell I, extending to 50°N, accounts for the strongest meridional mass transport, with the value at about $5.96 \times 10^{10}$ kg s$^{-1}$. Cells III-A and III-B are weaker and confined within the tropics, whose amplitude is just a third of that of the Cell I each. The annual-mean Hadley cells in the SH are similar to those in the NH but slightly stronger. The amplitude of Cell II is about $-7.90 \times 10^{10}$ kg s$^{-1}$, higher than that of Cell I. Cell IV is also stronger than Cell III, and its northern boundary extends to the NH, largely due to the strong temperature gradient between the Pacific ITCZ and East Pacific cold tongue. We also integrated Hadley Cells I, II, III-A/B, and IV-A/B along the zonal direction, and obtain an additive global HC. We found this "additive" circulation is identical to the traditional global HC, calculated by integrating the global zonal-mean meridional velocity (Figure 1).

Remarkably, the global HC in the NH (Figure 1) is significantly deeper and higher than that of the SH, largely due to the tropical SST gradient between the two hemispheres (Hou & Lindzen, 1992; Lindzen & Hou, 1988; Numaguti, 1995; Rind & Rossow, 1984; Schneider & Lindzen, 1977), given that the equatorial SST is relatively low over the Southeastern Pacific and the South Atlantic (cold tongue areas). Its horizontal distribution is also tightly associated with the zonal SST gradient along the equator, with deep atmospheric convection over warm SSTs and shallow circulation over the equatorial Pacific and Atlantic.

The traditional global HC shows a strong seasonality, motivating us to further investigate the seasonality of the Hadley cells in a regional perspective. As shown in Figure 3, the HC for all four seasons shares a similar horizontal structure, with four Hadley cells, except for the absence of Cells III and IV in the summer hemisphere (JJA in NH, and DJF in SH). Similar to the global HC, the regional Hadley cells show a clear seasonality, with the strongest cells usually appearing in the winter hemisphere (Dima & Wallace, 2003; Oort & Rasmusson, 1970; Oort & Yienger, 1996). In boreal winter (DJF), Cell I is responsible for a mass transport of about $14.3 \times 10^{10}$ kg s$^{-1}$, twice as much as its annual mean value. Similarly, over the Southern Hemisphere, Cell II is associated with about

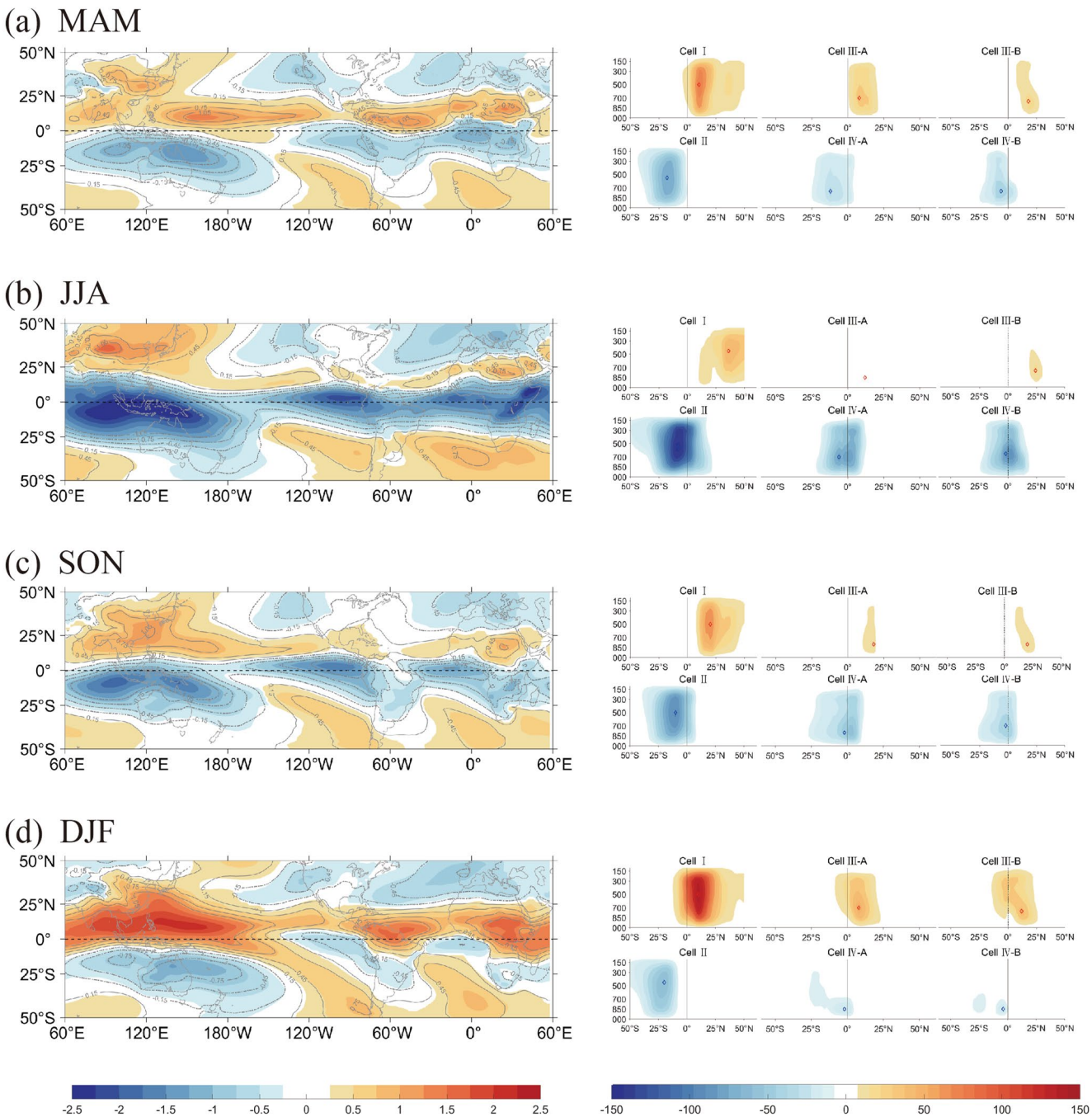


**Figure 3.** The horizontal and vertical spatial distribution of the seasonal regional Hadley circulation (HC). Left panels are the same as Figure 2a and right panels the same as Figure 2c, but for the four seasons.

$14.2 \times 10^{10}$ kg $s^{-1}$ of the mass transport in JJA. The Cells III and IV are relatively weaker than Cells I and II, and also show a clear seasonality. In particular, these two cells are extremely weak over the summer hemisphere (See Cell III in Figure 3b, and Cell IV in Figure 3d). This is primarily due to the relatively lower SST over the Eastern Pacific–Tropical Atlantic region and its induced weaker atmospheric convection (Cook, 2003; Lau et al., 1997; Zhang, 1993).

We further clarify the seasonality of the regional Hadley cells by performing an EOF decomposition based on the climatological states of the three-dimensional MSF with seasonal cycle-retained (Figure 4). The first EOF mode shows an equatorial asymmetric circulation pattern around the entire globe (Figures 4b and 4c), agreeing

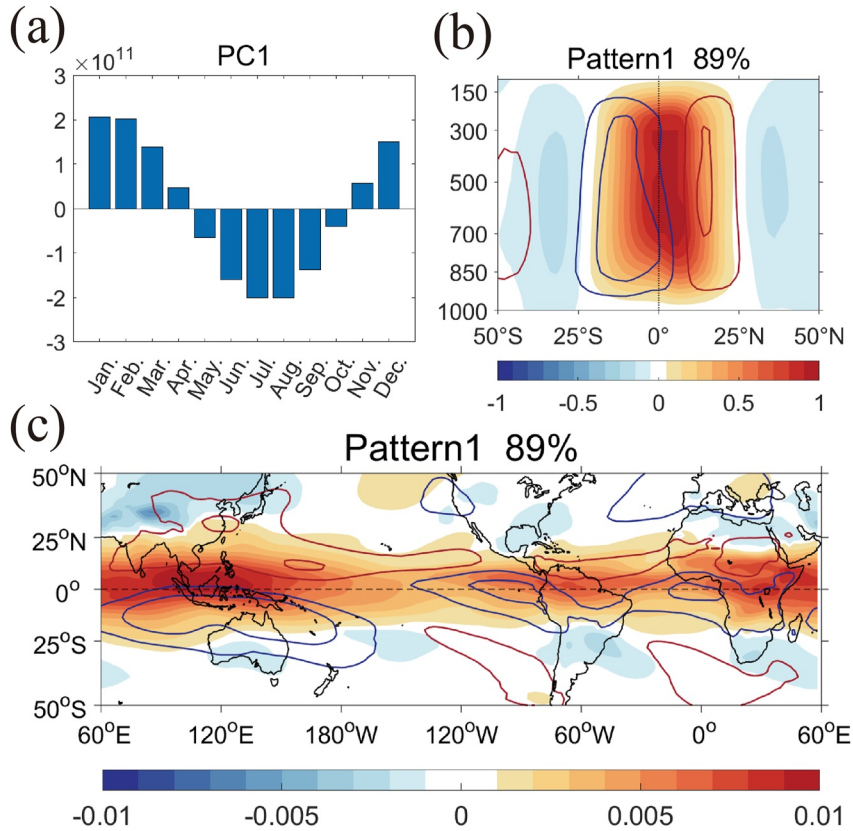


**Figure 4.** Empirical orthogonal function (EOF) decomposition of the three-dimensional mass stream function (MSF) with seasonal cycle-retained. (a) The time series of the first principal component. (b) The vertical distribution of the zonal integrated circulation of the EOF mode one (shading, unit is kg $s^{-1}$) and the climatology of the annual-mean MSF (contour interval is $4 \times 10^9$ kg $s^{-1}$, with red contours representing clockwise circulation, and blue contours indicating anti-clockwise circulation). (c) The horizontal distribution of mode one (shading, unit is kg $s^{-1}$) and the climatology of the annual-mean MSF (contour interval is $0.5 \times 10^9$ kg $s^{-1}$).

well with the previous study based on the zonally integrated MSF (Dima & Wallace, 2003), representing the seasonal cycle of the HC with a stronger and broader Hadley cell over the winter hemisphere (Figure 4). This cross-equatorial circulation is almost zonally homogeneous over the entire tropical region, despite that its branch over the IPWP region is relatively stronger, largely due to the strong variability of the deep atmospheric convection over that region.

We also demonstrate the horizontal distribution of the pressure level where the local MSF achieves its largest magnitude, at each grid point for all four seasons, representing the horizontal distribution of the height of the HC (Figure 5) and its seasonality. This horizontal distribution for different seasons shows very similar patterns to that in the annual mean field, with the highest center of the MSF (and deep convection) located over the western part of Cells I and II, namely the IPWP region. The eastern part of cells I and II, as well as cells III and IV are relatively shallower, whose MSF center is usually on the pressure level of about 700 hPa. This horizontal distribution is nearly identical in all four seasons, with almost no seasonality. It is mainly because that the height of the HC is associated with the height of the deep convection, primarily driven by the effective SST within the equatorial belt (15°S–15°N), which is not sensitive to seasons. As shown in Figure 6, there is deep atmospheric convection with strong convective precipitation over warm SST (>28°C) around the IPWP region and relatively shallower convection with relatively weaker precipitation over lower SST along the ITCZ (≈27°C) over the East Pacific and Tropical Atlantic. Given that the HC is a thermally driven circulation, the warm SST over the IPWP region generates a strong deep atmospheric convection (Figure 6) and thus essentially contributes to the upward branch of the regional HC, resulting in a pair of stronger and wider-extended Hadley cells around the IPWP region (Figure 6). In contrast, a relatively lower SST over the Eastern Pacific–Tropical Atlantic regions generates relatively shallower deep convection, resulting in weaker, thinner, and shallower cells around these regions.

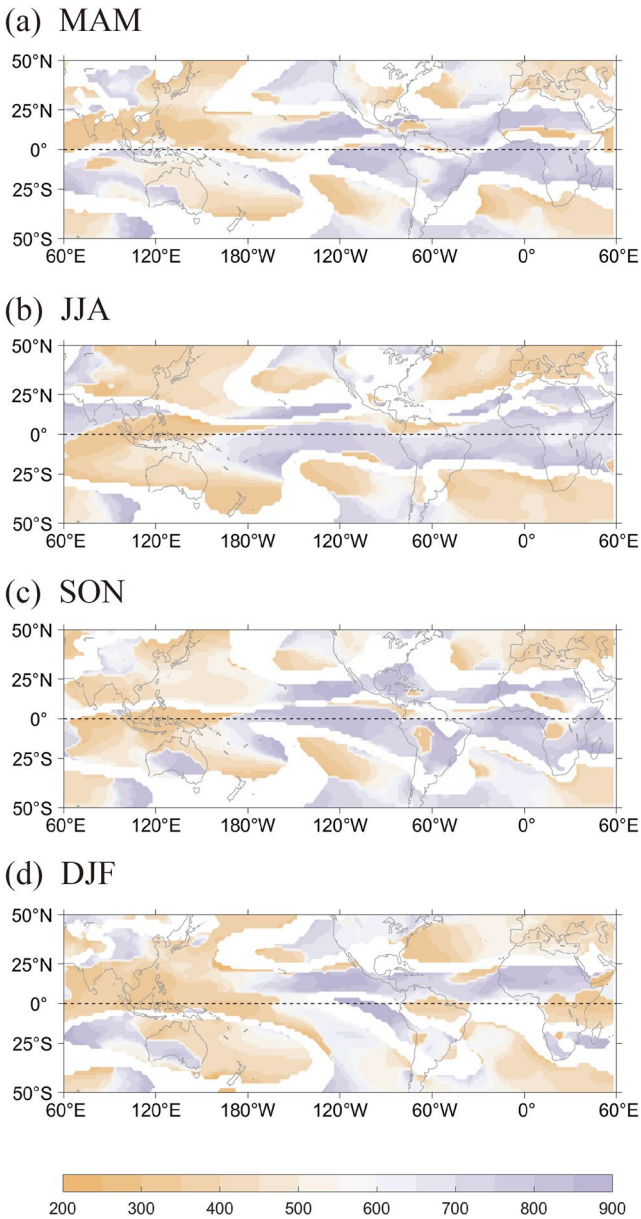


**Figure 5.** The height distribution (shading, unit is hPa) of the seasonal regional Hadley circulation (HC). As in Figure 2b, but for the four seasons.

## 4. Spread of HC Among Different Reanalyses

The above estimation is based on the ensemble mean of the eight reanalysis datasets. Here, we evaluate the quality and the uncertainty among these reanalyses in representing the HC and its three-dimensional distribution. We first calculate the horizontal distribution and the vertical structures of the global HC for each dataset (Figure 7). The eight datasets show similar MSF distributions in both horizontal and vertical structures, but the amplitudes of these patterns vary among these reanalyses. For example, CFSR, ERAI, and NCEP2 have stronger HC throughout the tropics (Figures 7b, 7c, and 7h), whereas 20CR, ERA5, MERRA, and MERRA2 are relatively weaker (Figures 7a, 7d, 7f, and 7g). In brief, the horizontal structure between different reanalyses is very similar, while a large spread exists in the amplitude of MSF among the eight reanalysis datasets.

We further quantify the coherency of the horizontal structure of these Hadley cells among different reanalysis datasets by calculating the spatial pattern correlation between each pair of the datasets including the ensemble-mean of all reanalyses (Figure 8a). The correlations between these datasets are always higher than 0.9, indicating that the horizontal structure of the regional HC among all these reanalysis datasets is nearly identical. In particular, the cross-correlation among all reanalyses except for NCEP2 and 20CR is higher than 0.95. The NCEP2 and 20CR are relatively poorly correlated with the other reanalyses ($r \approx 0.9$).

We further calculate the amplitude of each regional Hadley cell, together with the global HC over both hemispheres in all eight datasets, by comparing the maximum (minimum) values of the integrated MSF (Figure 8b). Results represent the magnitude of each cell as well as the global HC. The magnitude of the Northern Hemispheric global HC is from $6.92 \times 10^{10}$ to $10.86 \times 10^{10}$ kg s$^{-1}$, with an ensemble mean of $8.37 \times 10^{10}$ kg s$^{-1}$. While that of the Southern Hemisphere ranges from $-9.59 \times 10^{10}$ to $-14.51 \times 10^{10}$ kg s$^{-1}$, with an ensemble mean of $-11.93 \times 10^{10}$ kg s$^{-1}$ - about one-third stronger than the Northern Hemisphere HC.

The spread of regional Hadley cells among different reanalyses shows a similar feature to that of the global HC. More than half of the transport appears in Cells I (NH) and II (SH), with the magnitude ranging from $4.84 \times 10^{10}$ to $7.75 \times 10^{10}$ kg s$^{-1}$ (Cell I) and from $-6.94 \times 10^{10}$ to $-9.74 \times 10^{10}$ kg s$^{-1}$ (Cell II). The spreads of these cells are about 48.8% (Cell I) and 35.4% (Cell II) of the ensemble means over the Northern and Southern Hemispheres respectively. To further quantify the spread of the amplitudes of HC among different reanalyses, we calculate the coefficient of variation based on these datasets. It is 17% for the global HC, indicating large variations of the HC amplitudes among different datasets. Notably, we find that the Hadley cells in CFSR, ERAI, and NCEP2 are constantly stronger than that in the other datasets in both global and regional perspectives, reemphasizing the feature that different reanalysis datasets share similar spatial structure of the HC but with different amplitudes.

The magnitude of each Hadley cell represents a zonal integration of the local HC (MSF) at each longitude. In other words, either stronger local amplitude (of the Hadley cell) or broader horizontal distribution (of the Hadley cell) may increase the magnitude of the Hadley cell. We thus decompose the mass transport (Figure 8b) into two components, namely the local amplitude (Figure 9a) and the total area (Figure 9b). The spread of the local amplitude of each cell among different reanalyses is about 30%–50% of the ensemble mean, close to the spread of the magnitude (about 40%). Notably, a clear spread appears in the horizontal extent of the HC among different reanalyses. The spread of the total area of the HC among different datasets, within 30% of the peak value, is

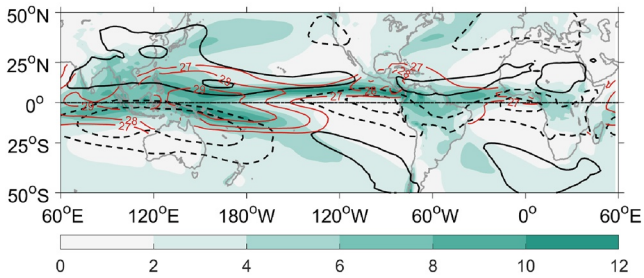


**Figure 6.** The climatology of the annual-mean precipitation (color shading, unit is mm day$^{-1}$) and sea surface temperature (SST) (red contours, unit is °C) based on ERSST. The four Hadley cells are also illustrated in this figure (black contours, with solid lines representing the positive mass stream function, and dashed curves representing the negative mass stream function).

about 41% and 30% of its ensemble mean in the Northern Hemisphere and Southern Hemisphere, respectively. This result highlights that the magnitude of each Hadley cell strongly depends on both the local amplitude and the horizontal extent, while a stronger cell is usually associated with a broader horizontal extension.

We further investigate the seasonality of the uncertainty of Hadley cells among different reanalyses by calculating the cross-spatial pattern correlation among different datasets (Figure 10) and quantifying the amplitudes of the magnitude (Figure 11) of each cell for the four seasons. Results show that the uncertainty of the regional HC among different datasets in each season shares similar characteristics with that of the annual mean states, all with strong cross-correlation among different datasets, but large spread in their amplitudes. The cross-correlation for MAM (Figure 10a) is lower than the other seasons, with a minimum value of about 0.85.

We further perform an EOF decomposition based on the climatological states of the three-dimensional MSF of different reanalysis datasets, to better retrieve the leading modes representing the spread of regional HC among these datasets. Figure 12 shows the horizontal patterns (Figures 12b and 12d) and the principal components (Figures 12a and 12c) of the first two modes, with the red and blue contours showing the EOF modes (which represent the leading spread modes) and the gray contours illustrating the climatological states of the ensemble mean of all reanalyses. The spatial pattern of Mode 1 matches the climatological state of the ensemble mean well, which reemphasizes the coherency of the horizontal distribution of the regional HC among different datasets and highlights that the first-order differences of the HC between different reanalyses are their global-mean amplitudes. Mode 2 shows a dipole pattern between the Maritime continent and the western tropical Pacific over both the Northern and Southern Hemispheres, which is associated with an eastward and westward shift of the Cells I and II respectively among different reanalyses.

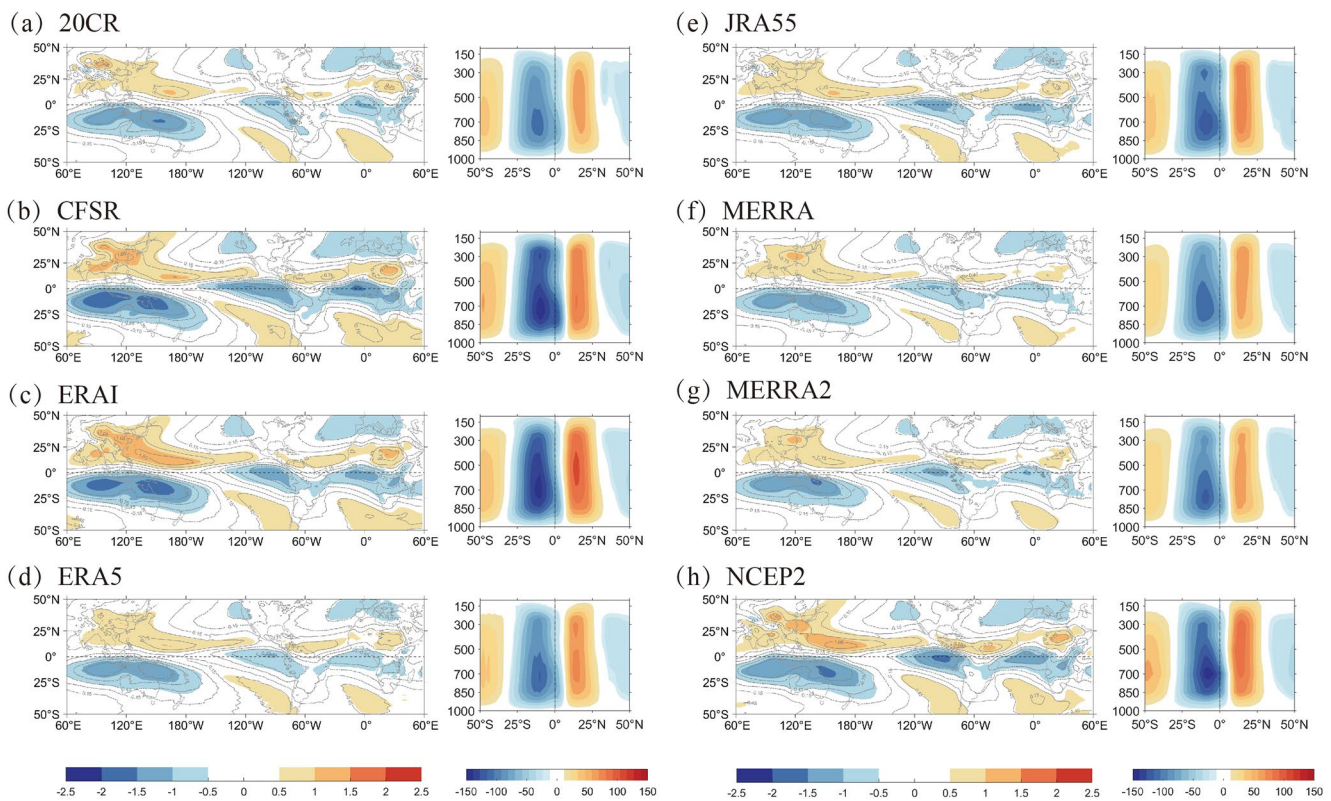


**Figure 7.** The horizontal distribution of the annual mean regional mass stream function (MSF) and the vertical distribution of the global MSF in the eight reanalysis datasets. Left panels of (a–h) same as Figure 2a, but for each reanalysis dataset. Right panels of (a–h) same as Figure 1, but for each reanalysis dataset.

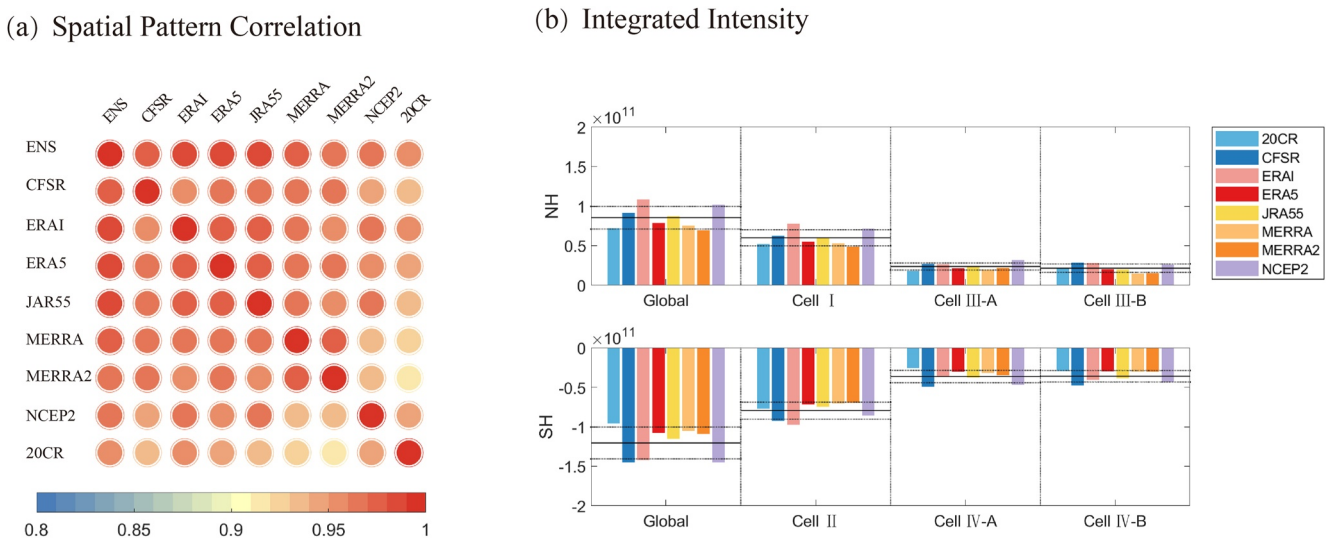


**Figure 8.** Quantification of the spread of the horizontal distribution of the annual mean regional mass stream function (MSF) and the globally integrated intensity and the Hadley cell among each reanalysis dataset. (a) The spatial pattern correlation between each pair of the eight reanalysis datasets including the ensemble-mean of all reanalyses. (b) The amplitude (kg $s^{-1}$) of the integrated MSF of the globe and each regional Hadley cell in each dataset. The solid lines show the amplitude of the multi-reanalysis ensemble. The dotted lines indicate ±1 standard deviation of the amplitude in the eight reanalyses.

We further project the PCs onto the precipitation field of the corresponding reanalyses through linear regression to elucidate the relationship between the diversities in the regional HC and precipitation (Figures 12b and 12d), with green colors indicating wet anomalies. PC1 is associated with a narrow, zonally quasi-symmetric anomalous precipitation belt near the equator, representing a stronger global-wide tropical convection in some of the reanalyses. This further implies that the discrepancy of the tropical precipitation among eight reanalysis datasets contributes to the spread of the amplitudes of the HC. In particular, the HC in CFSR, ERA-Interim, and NCEP2 is relatively stronger, while that of the 20CR, MERRA, and MERRA2 is relatively weaker.

PC2 shows a dipole-like circulation and precipitation pattern between the Maritime Continent and the tropical West Pacific, representing the difference in the location of the warm pool deep convection among these reanalyses. With a positive phase of the PC2 (e.g., the 20CR and NCEP2), the circulation as well as the precipitation is stronger over the West Pacific rather than the Maritime Continent area. With a negative phase of the PC2 (e.g., the CFSR, MERRA, and MERRA2), the circulation is relatively stronger over the Maritime continental rather than the West Pacific. This mode represents an eastward-westward shift of the convective precipitation and the regional HC among different reanalyses. In 20CR and NCEP2, the deep convection and the Hadley cells around the IPWP region shift to the east in comparison to that of the CFSR and MERRA.

We further analyze the multi-decadal trends of the regional HC and their diversity among different reanalysis datasets. Figure 13 shows the horizontal distribution of the multi-decadal trends of the regional MSF at each grid point based on different reanalysis datasets (considering that most of the reanalysis datasets start from 1979 or 1980, and ends in 2018–2022, we select the largest overlap of the time range of these reanalysis datasets: from 1980 to 2018. Only six reanalysis datasets: CFSR, ERA-Interim, ERA5, MERRA, JRA55, and NCEP2 are used in this analysis, in that the time range of the other reanalyses is relatively shorter). The horizontal distribution of the multi-decadal trend of the regional HC is very different from the horizontal distribution of the climatological state. Around the IPWP region, the HC is intensified during the past four decades (in most reanalyses except CFSR), represented as an anomalous positive MSF over the Northern Hemisphere and a negative MSF over the Southern Hemisphere (Figure 13a). In contrast, the HC is weakened over the Eastern Pacific in most of the reanalyses. These circulation changes are tightly related to the trend of the tropical SST forcing. In the past four decades since the 1980s, the tropical ocean experienced dipole-like SST changes, with warming trends over the Tropical Atlantic and the Indian Ocean, and La-Niña type SST changes (or negative phase of IPO) over the tropical Pacific. The warming trend over the IPWP region and the Tropical Atlantic intensifies the regional HC, while the cooling trend over the equatorial Eastern Pacific weakens the regional HC (Figure 13).

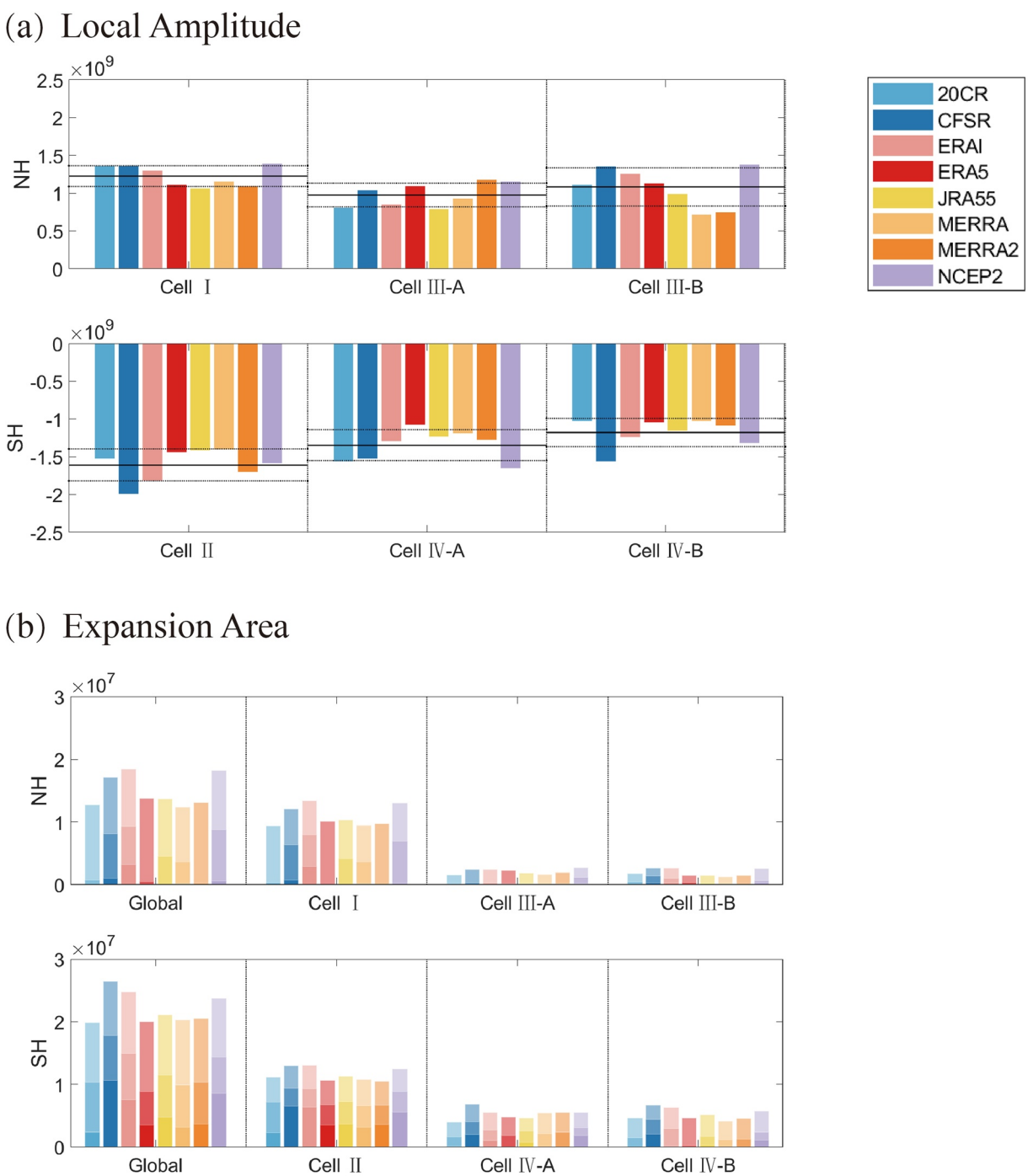


**Figure 9.** Same as Figure 8b but for the local amplitude and expansion area in the horizontal distribution. (a) The local amplitude (kg $s^{-1}$) in each dataset which is defined as the maximum or minimum value of each Hadley cell in the horizontal distribution. (b) The expansion area ($m^2$) of the globe and the Hadley cell in each dataset, with different shades of color representing the area within the 30%, 50%, and 70% of the peak value in the horizontal distribution respectively.

There is clear diversity of the regional HC trends among different reanalysis datasets. For example, CFSR shows a distinct horizontal distribution of the regional HC trend (Figure 13b), with a weakened HC over the IPWP region, opposite to that of the other reanalyses. The regional HC trends in NCEP2 are much stronger than that of the other reanalyses (Figure 13g). To quantify the spread of the trend among different reanalysis datasets, we further calculate the spatial pattern correlation of the regional HC trends among different datasets for the annual-mean

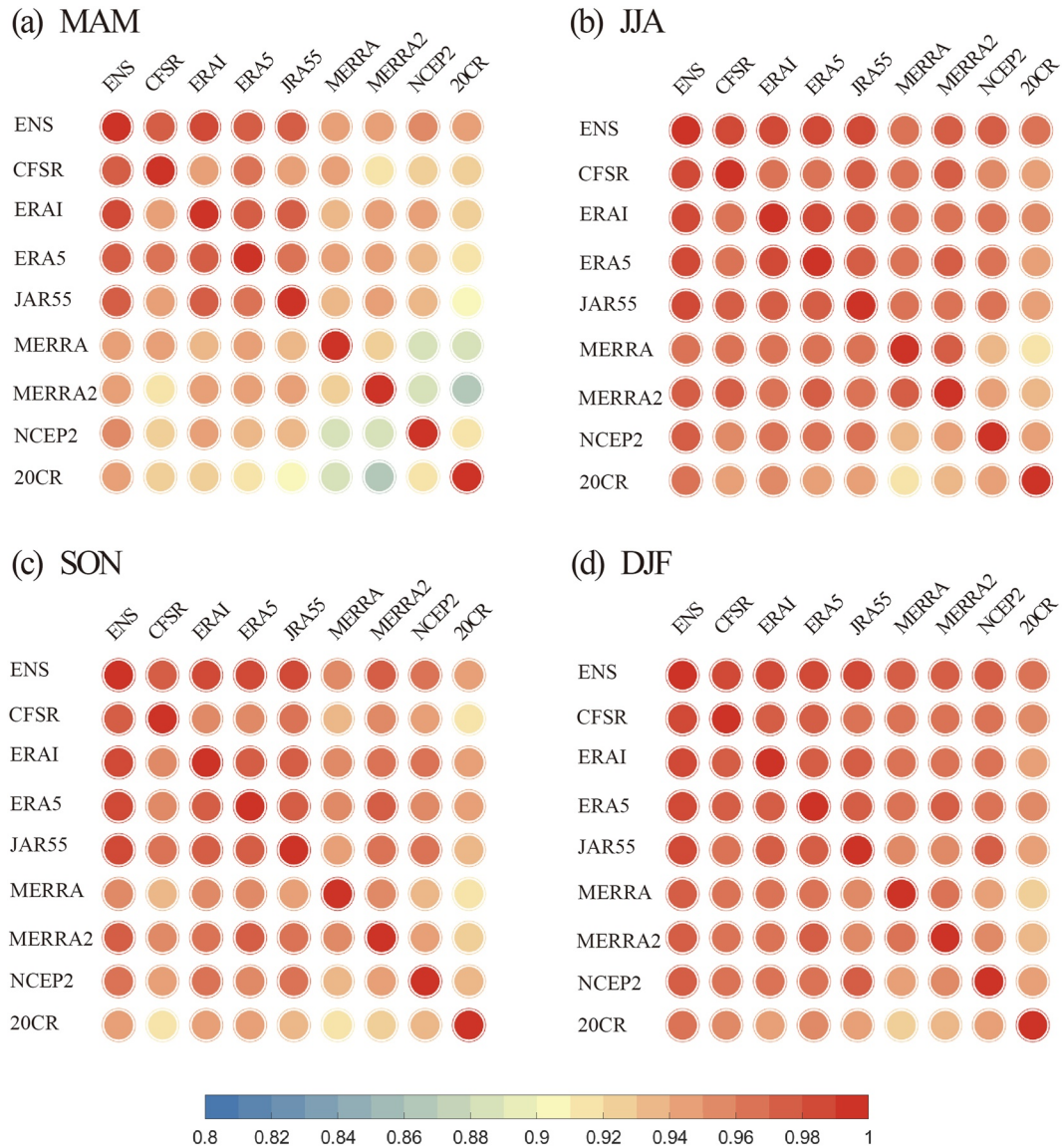


**Figure 10.** Same as Figure 8a but for the four seasons.

state, as well as for all four seasons, as shown in Figure 14. The correlations between each reanalysis dataset and the ensemble-mean of the six datasets are usually higher than 0.8, except for CFSR ($r \approx 0.3$).

According to the above analysis, the spatial structure of the regional HC trend in CFSR is distinct from that of other reanalyses, while the intensity of the regional HC trend in NCEP2 is much stronger. Among other reanalyses, the horizontal distributions of the regional HC trends are very similar.

## 5. Conclusions and Discussion

The HC, the dominant large-scale meridional overturning circulation over the tropics and subtropics, is usually defined using the global zonal-mean MSF derived from reanalyses rather than in situ observations. It is thus important to evaluate the uncertainty and spread of different reanalysis datasets in representing the HC. In addition, the MSF of HC is usually investigated in a global perspective, preventing us from a thorough understanding of the detailed spatial structure of this large-scale circulation.

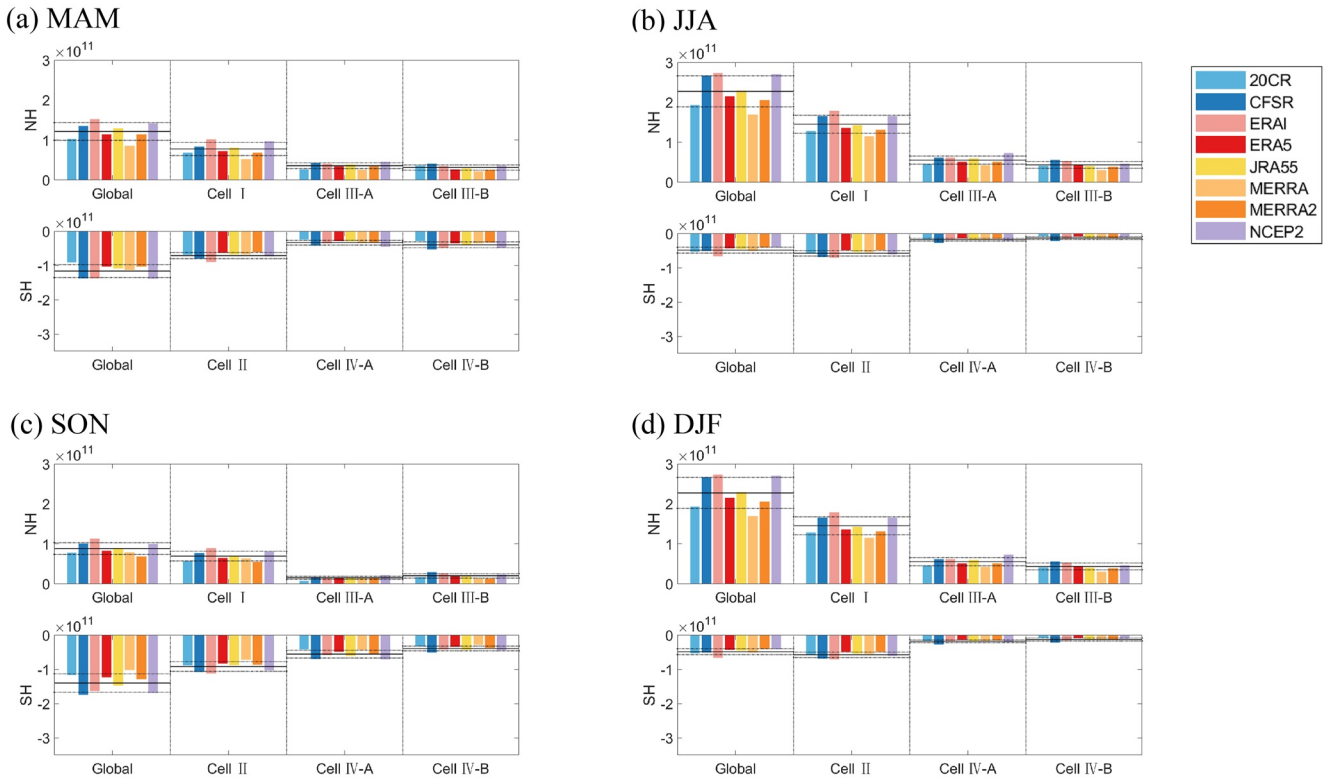


**Figure 11.** Same as Figure 8b but for the four seasons.

In this study, we evaluate the spread among eight commonly used reanalysis datasets in terms of their ability to represent the global and regional HC. We first calculate a local MSF of the HC at each longitude, to illustrate the three-dimensional structure of the global HC. We then divide the HC into four cells based on the natural boundaries of the MSF, namely the Cell I, II, III, and IV, with the latter two each further divided into two sub-cells. We further evaluate the coherency and spread of both the amplitudes and the spatial structure of the HC among reanalysis datasets through multiple statistical analyses including spatial pattern correlation, EOF decomposition, and the quantification of the intensity and expansion of each cell. Results show that the spatial distributions of the HC are almost identical among different datasets, with a cross-spatial pattern correlation of about 0.95 between each pair of datasets. However, the amplitudes of the HC vary strongly among different datasets, with a spread about two fifths of the ensemble mean. In particular, the amplitudes of the HC in CFSR, ERAI and NCEP2 are much larger than the other datasets over all three ocean basins. The first EOF mode of the MSF among different ensemble members has a spatial pattern almost identical to the ensemble mean HC, reaffirming that the inter-dataset differences are dominated by the magnitude differences of HC.

Further analysis reveals that this spread of the HC amplitude may be associated with the tropical precipitation biases among different datasets. However, the relationship between precipitation and HC is complicated. The EOF decomposition shows that both the amplitudes and the relative zonal location of the Hadley cells may be tightly associated with the tropical precipitation, which requires an in-depth investigation.

We also investigate the vertical distribution of these regional Hadley cells. Results show that Cells I and II, centered at the Indo-Pacific warm pool region, are usually higher than others, with the maximum MSF value located at the level of ∼500 hPa. Other cells over the East Pacific and the Atlantic (Cell III-A and III-B, Cell IV-A and IV-B) are relatively lower, whose maximum MSF is located at ∼700 hPa. These spatial variations in the vertical structure of circulation may be primarily attributed to the horizontal distribution of the SST. Over warm SST region (e.g., the Indo-Pacific warm pool region), deep atmospheric convection drives the circulation of the first baroclinic mode, while over cold SST region (the cold tongue region), deep convection is suppressed. In the Western Hemisphere, the ITCZ is displaced north of the equator, where the upward motion is fed by the southeasterly trade winds from the south of the equator. The southeasterly trades are confined to the planetary

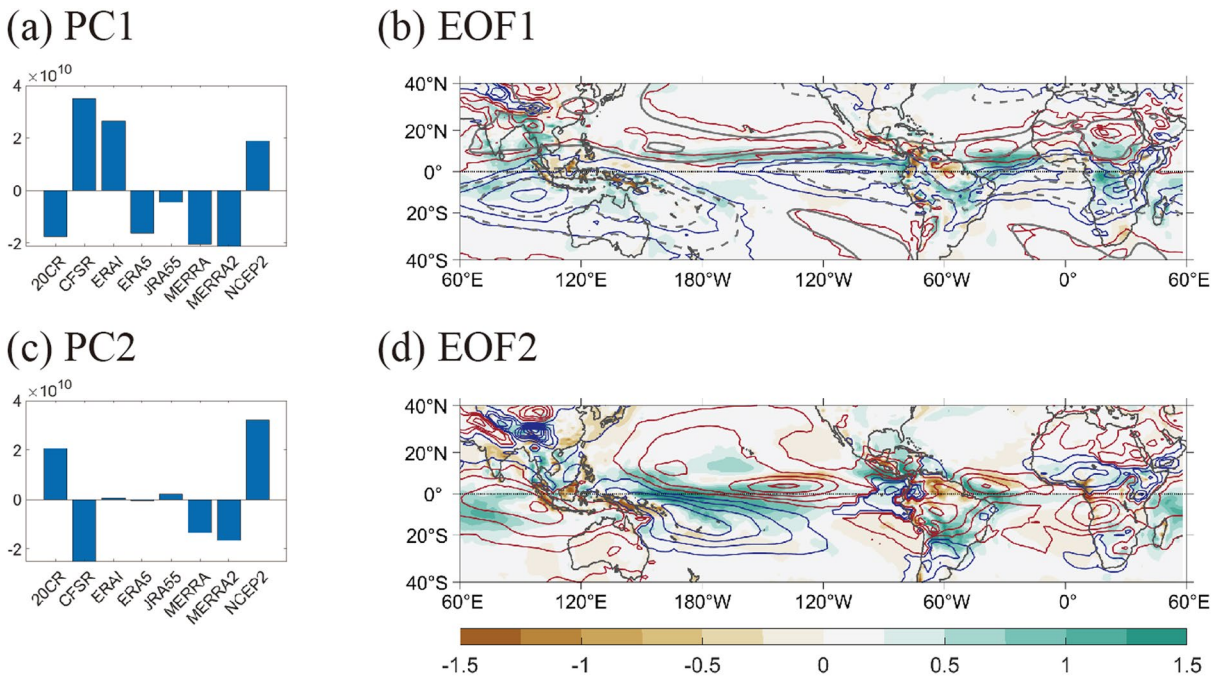


**Figure 12.** Empirical orthogonal function (EOF) decomposition of the three-dimensional MSF in annual mean among the eight reanalysis datasets. Left panels (a, c) show the principal components of the first two modes. Right panels (b, d) show the circulation and the precipitation of the first two modes, respectively. The regression patterns of the precipitation against the standardized PC1 and PC2 are illustrated by color shading (Green colors indicate the wet anomalies, with a unit of mm day$^{-1}$). Red and blue contours show the anomalous mass stream function (MSF) associated with Mode 1 and 2, (contour interval is 0.0025 kg s$^{-1}$, with red contours indicating positive value, and blue contours indicating negative one). The climatology states of the MSF are shown in (b) with gray contours (contour interval is $0.5 \times 10^9$ kg s$^{-1}$ with solid contours indicating positive values, and dashed contours indicating negative ones).

boundary layer capped by an inversion. The northward SST gradient drives a shallow overturning cell superimposed on a deep one that feeds the ITCZ (Back & Bretherton, 2006; Small et al., 2005).

We further examine the trends of the regional HC and their spread among six reanalysis datasets during the period from 1980 to 2018. In the past four decades, the HC has been intensified over the IPWP region, but weakened over the Eastern Pacific, which are related to a La-Niña type SST changes over the tropical Pacific. However, the horizontal distribution of regional HC trend in CFSR is different, with a weakened HC over the IPWP region. Meanwhile, the trend in NCEP2 is much stronger. Except for CFSR, the other five reanalyses share a similar spatial structure of the regional HC trends, with a spatial-pattern correlation coefficient higher than 0.8 between each pair of reanalysis datasets. Unlike its climatological states, the spatial structures of the regional HC trends show distinct features among different reanalyses datasets. Considering that the regional HC plays a crucial role in the mass and energy transport between tropics and higher latitudes, it is important to further evaluate the capability of different datasets in capturing the long-term trend of the regional HC, which will be a main focus of our future study.

HC plays a key role in transporting mass, moisture, and energy between the tropics and higher latitudes. However, it is very hard to observe HC directly through in situ measurements or remote sensing. Till now, the reanalysis dataset is an optimal alternative in reconstructing the HC and is broadly used in previous studies as a proxy of observations. Our results suggest that, although the spatial structure of the HC is nearly identical in all reanalyses, the uncertainty in these datasets is non-negligible when studying the HC, given the large spread in the HC amplitudes among these datasets. There is thus an urgent need to further evaluate the quality of each dataset, and to achieve an optimized estimation of the global HC and its changes. Numerical simulation experiments may provide another perspective in reproducing the HC (Cheng et al., 2020; Feng et al., 2015; Guo, Li, Feng, et al., 2016; Wang et al., 2020).

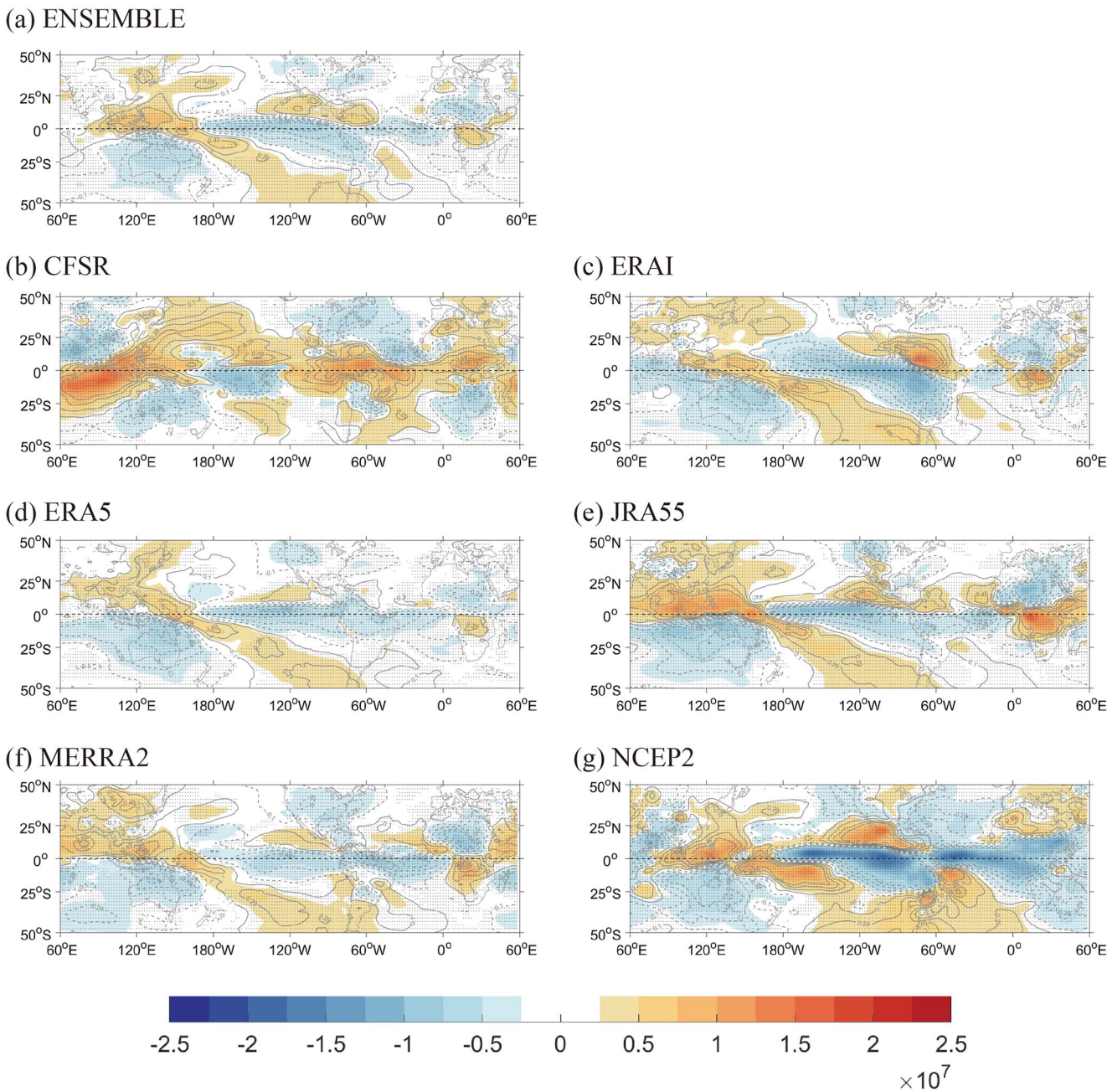


**Figure 13.** The horizontal distribution of the maximum intensities (in the vertical profile above each grid) of the trend (1980–2018) of three-dimensional mass stream function (MSF; shading, kg $s^{-1}$) based on the ensemble-mean and the six reanalysis datasets.

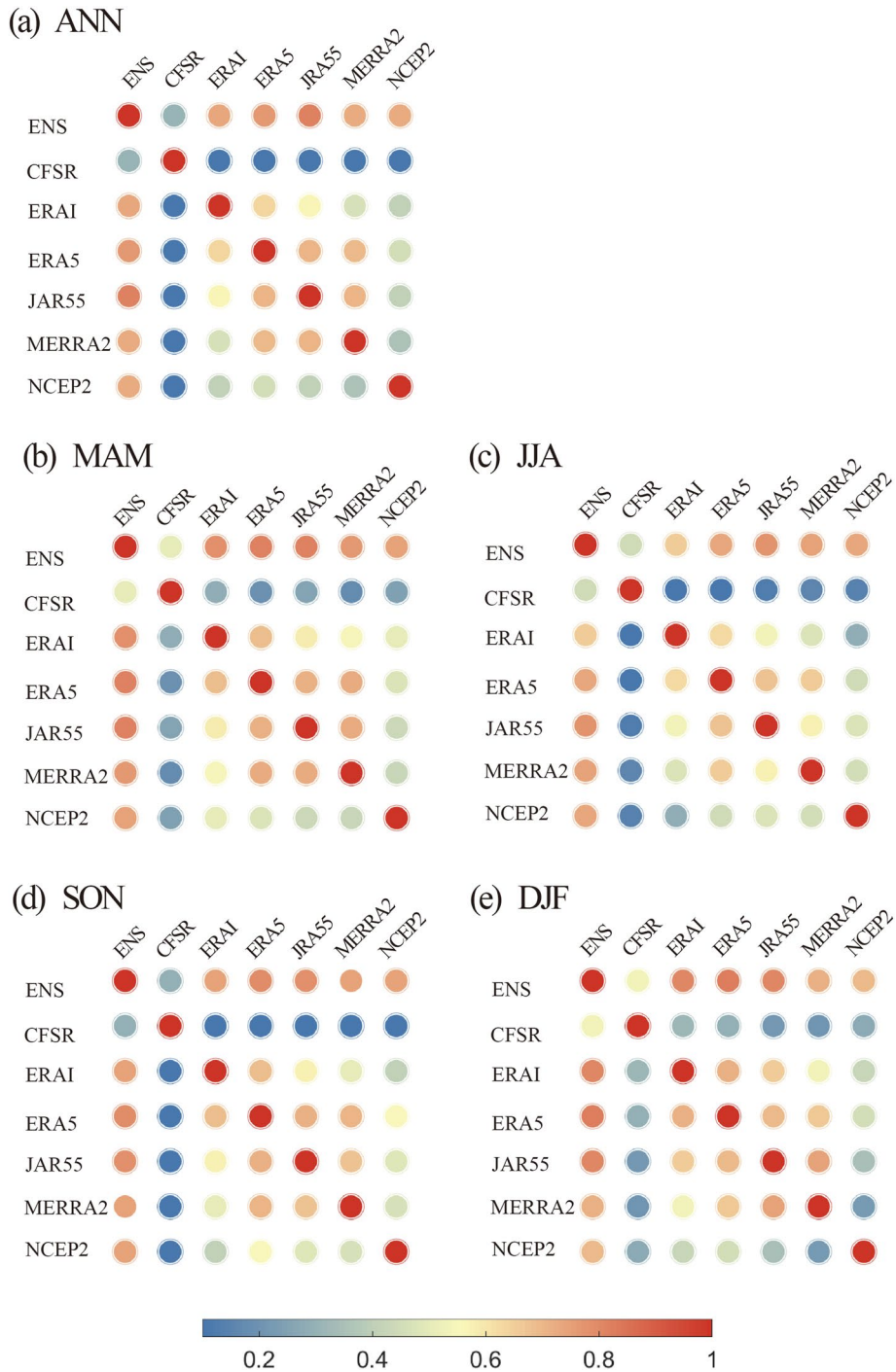


**Figure 14.** Same as Figure 8a but for the trend of the regional mass stream function (MSF; for annual-mean and all four seasons).

## Data Availability Statement

20CR reanalysis data (Compo et al., 2011) is available at https://psl.noaa.gov/data/20thC_Rean/. CFSR reanalysis data (Saha et al., 2010) is obtained from the National Climatic Data Center (NCDC) and NCAR at https://rda.ucar.edu/datasets/ds093.2/. ERA-Interim (Dee et al., 2011) and ERA5 (Hersbach et al., 2020) reanalysis data are produced by the European Center for Medium-Range Weather Forecasts (ECWMF) and are accessible

at https://www.ecmwf.int/en/forecasts/datasets/. JRA55 reanalysis data (Kobayashi et al., 2015) is provided by the Japan Meteorological Agency, which is available from http://search.diasjp.net/en/dataset/JRA55. MERRA (Rienecker et al., 2011) and MERRA2 (Gelaro et al., 2017) are provided by NASA's Global Modeling and Assimilation Office at https://disc.gsfc.nasa.gov/. NCEP2 reanalysis data (Kanamitsu et al., 2002) is provided by the NCEP and NCAR at https://psl.noaa.gov/data/gridded/data.ncep.reanalysis2.html. ERSST data (Huang et al., 2017) is available from International Comprehensive Ocean-Atmosphere Data Set (ICOADS) at https://psl.noaa.gov/data/gridded/data.noaa.ersst.v5.html. The calculation of the mass stream function is done with the NCAR Command Language (NCL) version 6.6.2 (NCAR, 2019), which is available from https://www.ncl.ucar.edu/. Further data analysis and figures are made with Matlab version R2018a (Mathworks Inc., 2020), accessible at https://in.mathworks.com/products/matlab.html.

**Acknowledgments**
The authors thank the editor and the three anonymous reviewers for their constructive suggestions, which largely improve the manuscript. Yadi Li and Xichen Li were supported by the Strategic Priority Research Program of the Chinese Academy of Sciences (Grant XDA19070202), and the National Natural Science Foundation of China (Grants 41976193 and 41676190). Shang-Ping Xie was supported by the National Science Foundation (AGS-2105654). Gan Zhang was supported by Princeton University's Cooperative Institute for Modeling the Earth system, through the Predictability and Explaining Extremes Initiative. Zhuo Wang was supported by the National Oceanic and Atmospheric Administration (NOAA) (Grant NA18OAR4310271).

## References

Allen, R. J., Norris, J. R., & Kovilakam, M. (2014). Influence of anthropogenic aerosols and the Pacific Decadal Oscillation on tropical belt width. *Nature Geoscience*, *7*(4), 270–274. https://doi.org/10.1038/NGEO2091

Amaya, D. J., Siler, N., Xie, S.-P., & Miller, A. J. (2017). The interplay of internal and forced modes of Hadley cell expansion: Lessons from the global warming hiatus. *Climate Dynamics*, *51*(1–2), 305–319. https://doi.org/10.1007/s00382-017-3921-5

Back, L. E., & Bretherton, C. S. (2006). Geographic variability in the export of moist static energy and vertical motion profiles in the tropical Pacific. *Geophysical Research Letters*, *33*(17), L17810. https://doi.org/10.1029/2006gl026672

Bjerknes, J. (1966). A possible response of the atmospheric Hadley circulation to equatorial anomalies of ocean temperature. *Tellus*, *18*(4), 820–829. https://doi.org/10.1111/j.2153-3490.1966.tb00303.x

Chen, S., Wei, K., Chen, W., & Song, L. (2014). Regional changes in the annual mean Hadley circulation in recent decades. *Journal of Geophysical Research: Atmospheres*, *119*(13), 7815–7832. https://doi.org/10.1002/2014jd021540

Cheng, J., Hu, S., Gao, C., Hou, X., Xu, Z., & Feng, G. (2020). On the discrepancies in the changes in the annual mean Hadley circulation among different regions and between CMIP5 models and reanalyses. *Theoretical and Applied Climatology*, *141*(3–4), 1475–1491. https://doi.org/10.1007/s00704-020-03292-3

Compo, G. P., Whitaker, J. S., Sardeshmukh, P. D., Matsui, N., Allan, R. J., Yin, X., et al. (2011). The twentieth-century reanalysis project. *Quarterly Journal of the Royal Meteorological Society*, *137*(654), 1–28. https://doi.org/10.1002/qj.776

Cook, K. H. (2003). Role of continents in driving the Hadley cells. *Journal of the Atmospheric Sciences*, *60*(7), 957–976. https://doi.org/10.1175/1520-0469(2003)060<0957:rocidt>2.0.co;2

Davis, S. M., & Rosenlof, K. H. (2012). A multidiagnostic intercomparison of tropical-width time series using reanalyses and satellite observations. *Journal of Climate*, *25*(4), 1061–1078. https://doi.org/10.1175/jcli-d-11-00127.1

Dee, D. P., Uppala, S. M., Simmons, A., Berrisford, P., Poli, P., Kobayashi, S., et al. (2011). The ERA-Interim reanalysis: Configuration and performance of the data assimilation system. *Quarterly Journal of the Royal Meteorological Society*, *137*(656), 553–597. https://doi.org/10.1002/qj.828

Diaz, H. F., & Bradley, R. S. (2004). The Hadley circulation: Present, past, and future—An introduction. *Advances in Global Change Research*, *21*, 1–5. https://doi.org/10.1007/978-1-4020-2944-8_1

Dima, I. M., & Wallace, J. M. (2003). On the seasonality of the Hadley cell. *Journal of the Atmospheric Sciences*, *60*(12), 1522–1527. https://doi.org/10.1175/1520-0469(2003)060<1522:OTSOTH>2.0.CO;2

Feng, J., Li, J., Jin, F., Zhao, S., & Xie, F. (2017). The responses of the Hadley circulation to different meridional SST structures in the seasonal cycle. *Journal of Geophysical Research: Atmospheres*, *122*(15), 7785–7799. https://doi.org/10.1002/2017jd026953

Feng, J., Li, J., Jin, F., Zhao, S., & Zhu, J. (2018). Relationship between the Hadley circulation and different tropical meridional SST structures during boreal summer. *Journal of Climate*, *31*(16), 6575–6590. https://doi.org/10.1175/jcli-d-18-0095.1

Feng, J., Li, J., Zhu, J., Li, F., & Sun, C. (2015). Simulation of the equatorially asymmetric mode of the Hadley circulation in CMIP5 models. *Advances in Atmospheric Sciences*, *32*(8), 1129–1142. https://doi.org/10.1007/s00376-015-4157-0

Feng, J., Zhu, J., & Li, F. (2016). Climatological vertical features of Hadley circulation depicted by the NCEP/NCAR, ERA40, NCEP-DOE, JRA25, ERA-Interim, and CFSR reanalyses. *Sola*, *12*(0), 237–241. https://doi.org/10.2151/sola.2016-047

Freitas, A. C. V., Aímola, L., Ambrizzi, T., & de Oliveira, C. P. (2016). Changes in intensity of the regional Hadley cell in Indian Ocean and its impacts on surrounding regions. *Meteorology and Atmospheric Physics*, *129*(3), 229–246. https://doi.org/10.1007/s00703-016-0477-6

Frierson, D. M. W., Lu, J., & Chen, G. (2007). Width of the Hadley cell in simple and comprehensive general circulation models. *Geophysical Research Letters*, *34*(18), L18804. https://doi.org/10.1029/2007gl031115

Fu, Q., Johanson, C. M., Wallace, J. M., & Reichler, T. (2006). Enhanced mid-latitude tropospheric warming in satellite measurements. *Science*, *312*(5777), 1179. https://doi.org/10.1126/science.1125566

Fu, Q., & Lin, P. (2011). Poleward shift of subtropical jets inferred from satellite-observed lower-stratospheric temperatures. *Journal of Climate*, *24*(21), 5597–5603. https://doi.org/10.1175/jcli-d-11-00027.1

Gelaro, R., McCarty, W., Suárez, M. J., Todling, R., Molod, A., Takacs, L., et al. (2017). The Modern-Era Retrospective analysis for Research and Applications, version 2 (MERRA-2). *Journal of Climate*, *30*(14), 5419–5454. https://doi.org/10.1175/JCLI-D-16-0758.1

Grise, K. M., Davis, S. M., Staten, P. W., & Adam, O. (2018). Regional and seasonal characteristics of the recent expansion of the tropics. *Journal of Climate*, *31*(17), 6839–6856. https://doi.org/10.1175/jcli-d-18-0060.1

Guo, Y.-P., Li, J.-P., & Feng, J. (2016). Climatology and interannual variability of the annual mean Hadley circulation in CMIP5 models. *Advances in Climate Change Research*, *7*(1–2), 35–45. https://doi.org/10.1016/j.accre.2016.04.005

Guo, Y.-P., Li, J.-P., Feng, J., Xie, F., Sun, C., & Zheng, J. (2016). The multidecadal variability of the asymmetric mode of the boreal autumn Hadley circulation and its link to the Atlantic multidecadal oscillation. *Journal of Climate*, *29*(15), 5625–5641. https://doi.org/10.1175/jcli-d-15-0025.1

Hadley, G. (1735). Concerning the cause of the general trade winds. *Philosophical Transactions of the Royal Society*, *39*, 58–62. https://doi.org/10.1098/rstl.1735.0014

Held, I. M. (2001). The partitioning of the poleward energy transport between the tropical ocean and atmosphere. *Journal of the Atmospheric Sciences*, *58*(8), 943–948. https://doi.org/10.1175/1520-0469(2001)058<0943:TPOTPE>2.0.CO;2

Held, I. M., & Hou, A. Y. (1980). Nonlinear axially symmetric circulations in a nearly inviscid atmosphere. *Journal of the Atmospheric Sciences*, *37*(3), 515–533. https://doi.org/10.1175/1520-0469(1980)037<0515:nascia>2.0.co;2;2

Hersbach, H., Bell, B., Berrisford, P., Hirahara, S., Horányi, A., Muñoz-Sabater, J., et al. (2020). The ERA5 global reanalysis. *Quarterly Journal of the Royal Meteorological Society*, *146*(730), 1999–2049. https://doi.org/10.1002/qj.3803

Hou, A. Y. (1998). Hadley circulation as a modulator of the extratropical climate. *Journal of the Atmospheric Sciences*, *55*(14), 2437–2457. https://doi.org/10.1175/1520-0469(1998)055<2437:Hcaamo>2.0.Co;2

Hou, A. Y., & Lindzen, R. S. (1992). The influence of concentrated heating on the Hadley circulation. *Journal of the Atmospheric Sciences*, *49*(14), 1233–1241. https://doi.org/10.1175/1520-0469(1992)049<1233:tiocho>2.0.co;2

Hu, Y., & Fu, Q. (2007). Observed poleward expansion of the Hadley circulation since 1979. *Atmospheric Chemistry and Physics Discussions*, *7*. https://doi.org/10.5194/acpd-7-9367-2007

Huang, B., Thorne, P. W., Banzon, V. F., Boyer, T., Chepurin, G., Lawrimore, J. H., et al. (2017). Extended Reconstructed Sea Surface Temperature, Version 5 (ERSSTv5): Upgrades, validations, and intercomparisons. *Journal of Climate*, *30*(20), 8179–8205. https://doi.org/10.1175/jcli-d-16-0836.1

Huang, R., Chen, S., Chen, W., & Hu, P. (2018). Interannual variability of regional Hadley circulation intensity over western Pacific during boreal winter and its climatic impact over Asia-Australia region. *Journal of Geophysical Research: Atmospheres*, *123*(1), 344–366. https://doi.org/10.1002/2017jd027919

Huang, R., Chen, S., Chen, W., Hu, P., & Yu, B. (2019). Recent strengthening of the regional Hadley circulation over the western Pacific during boreal spring. *Advances in Atmospheric Sciences*, *36*(11), 1251–1264. https://doi.org/10.1007/s00376-019-9004-2

Johanson, C. M., & Fu, Q. (2009). Hadley cell widening: Model simulations versus observations. *Journal of Climate*, *22*(10), 2713–2725. https://doi.org/10.1175/2008jcli2620.1

Kamae, Y., Li, X., Xie, S.-P., & Ueda, H. (2017). Atlantic effects on recent decadal trends in global monsoon. *Climate Dynamics*, *49*(9–10), 1–13. https://doi.org/10.1007/s00382-017-3522-3

Kanamitsu, M., Ebisuzaki, W., Woollen, J., Yang, S.-K., Hnilo, J., Fiorino, M., & Potter, G. (2002). NCEP-DOE AMIP-II reanalysis (R-2). *Bulletin of the American Meteorological Society*, *83*(11), 1631–1644. https://doi.org/10.1175/BAMS-83-11-1631

Kim, Y. H., Min, S. K., Son, S. W., & Choi, J. (2017). Attribution of the local Hadley cell widening in the Southern Hemisphere. *Geophysical Research Letters*, *44*(2), 1015–1024. https://doi.org/10.1002/2016gl072353

Kobayashi, S., Ota, Y., Harada, Y., Ebita, A., Moriya, M., Onoda, H., et al. (2015). The JRA-55 reanalysis: General specifications and basic characteristics. *Journal of the Meteorological Society of Japan. Series II*, *93*(1), 5–48. https://doi.org/10.2151/jmsj.2015-001

Lau, K. M., Wu, H. T., & Bony, S. (1997). The role of large-scale atmospheric circulation in the relationship between tropical convection and sea surface temperature. *Journal of Climate*, *10*(3), 381–392. https://doi.org/10.1175/1520-0442(1997)010<0381:TROLSA>2.0.CO;2

Lindzen, R. S. (1994). Climate dynamics and global change. *Annual Review of Fluid Mechanics*, *26*(1), 353–378. https://doi.org/10.1146/annurev.fl.26.010194.002033

Lindzen, R. S., & Hou, A. V. (1988). Hadley circulations for zonally averaged heating centered off the equator. *Journal of the Atmospheric Sciences*, *45*(17), 2416–2427. https://doi.org/10.1175/1520-0469(1988)045<2416:HCFZAH>2.0.CO;2

Lu, J., Chen, G., & Frierson, D. M. W. (2008). Response of the zonal mean atmospheric circulation to El Niño versus global warming. *Journal of Climate*, *21*(22), 5835–5851. https://doi.org/10.1175/2008jcli2200.1

Lu, J., Deser, C., & Reichler, T. (2009). Cause of the widening of the tropical belt since 1958. *Geophysical Research Letters*, *36*(3). https://doi.org/10.1029/2008gl036076

Lu, J., Vecchi, G. A., & Reichler, T. (2007). Expansion of the Hadley cell under global warming. *Geophysical Research Letters*, *34*(6), L06805. https://doi.org/10.1029/2006gl028443

Mathew, S. S., Kumar, K. K., & Subrahmanyam, K. V. (2016). Hadley cell dynamics in Japanese reanalysis-55 dataset: Evaluation using other reanalysis datasets and global radiosonde network observations. *Climate Dynamics*, *47*(12), 3917–3930. https://doi.org/10.1007/s00382-016-3051-5

Mathworks Inc. (2018). Matlab [Software]. Mathworks Inc. Retrieved from https://in.mathworks.com/products/matlab.html

NCAR. (2019). The NCAR Command Language (version 6.6.2) [Software]. UCAR/NCAR/CISL/TDD. https://10.5065/D6WD3XH5

Nguyen, H., Hendon, H. H., Lim, E. P., Boschat, G., Maloney, E., & Timbal, B. (2017). Variability of the extent of the Hadley circulation in the Southern Hemisphere: A regional perspective. *Climate Dynamics*, *50*(1–2), 129–142. https://doi.org/10.1007/s00382-017-3592-2

Nguyen, H., Lucas, C., Evans, A., Timbal, B., & Hanson, L. (2015). Expansion of the Southern Hemisphere Hadley cell in response to greenhouse gas forcing. *Journal of Climate*, *28*(20), 8067–8077. https://doi.org/10.1175/JCLI-D-15-0139.1

Numaguti, A. (1995). Dynamics and energy balance of the Hadley circulation and the tropical precipitation zones. Part II: Sensitivity to meridional SST distribution. *Journal of the Atmospheric Sciences*, *52*(8), 1128–1141. https://doi.org/10.1175/1520-0469(1995)052<1128:daebot>2.0.co;2

Oort, A. H., & Rasmusson, E. M. (1970). On the annual variation of the monthly mean meridional circulation. *Monthly Weather Review*, *98*(6), 423–442. https://doi.org/10.1175/1520-0493(1970)098<0423:OTAVOT>2.3.CO;2

Oort, A. H., & Yienger, J. J. (1996). Observed interannual variability in the Hadley circulation and its connection to ENSO. *Journal of Climate*, *9*(11), 2751–2767. https://doi.org/10.1175/1520-0442(1996)009<2751:OIVITH>2.0.CO;2

Previdi, M., & Liepert, B. G. (2007). Annular modes and Hadley cell expansion under global warming. *Geophysical Research Letters*, *34*(22), L22701. https://doi.org/10.1029/2007gl031243

Quan, X.-W., Diaz, H. F., & Hoerling, M. P. (2004). Change in the tropical Hadley cell since 1950. In *The Hadley circulation: Present, past, and future* (pp. 85–120). Springer. https://doi.org/10.1007/978-1-4020-2944-8_4

Rienecker, M. M., Suarez, M. J., Gelaro, R., Todling, R., Bacmeister, J., Liu, E., et al. (2011). MERRA: NASA's Modern-Era Retrospective analysis for Research and Applications. *Journal of Climate*, *24*(14), 3624–3648. https://doi.org/10.1175/JCLI-D-11-00015.1

Rind, D., & Rossow, W. B. (1984). The effects of physical processes on the Hadley circulation. *Journal of the Atmospheric Sciences*, *41*(4), 479–507. https://doi.org/10.1175/1520-0469(1984)041<0479:teoppo>2.0.co;2

Rossignolstrick, M. (1983). African monsoons, an immediate climate response to orbital insolation. *Nature*, *304*(5921), 46–49. https://doi.org/10.1038/304046a0

Saha, S., Moorthi, S., Pan, H.-L., Wu, X., Wang, J., Nadiga, S., et al. (2010). The NCEP climate forecast system reanalysis. *Bulletin of the American Meteorological Society*, *91*(8), 1015–1058. https://doi.org/10.1175/2010BAMS3001.1

Schneider, E. K., & Lindzen, R. S. (1977). Axially symmetric steady-state models of the basic state for instability and climate studies. Part I. Linearized calculations. *Journal of the Atmospheric Sciences*, *34*(2), 263–279. https://doi.org/10.1175/1520-0469(1977)034<0263:asssmo>2.0.co;2

Seager, R., Harnik, N., Kushnir, Y., Robinson, W., & Miller, J. (2003). Mechanisms of hemispherically symmetric climate variability. *Journal of Climate*, *16*(18), 2960–2978. https://doi.org/10.1175/1520-0442(2003)016<2960:mohscv>2.0.co;2;2

Small, R. J., Xie, S.-P., Wang, Y., Esbensen, S. K., & Vickers, D. (2005). Numerical simulation of boundary layer structure and cross-equatorial flow in the Eastern Pacific. *Journal of the Atmospheric Sciences*, *62*(6), 1812–1830. https://doi.org/10.1175/JAS3433.1

Stachnik, J. P., & Schumacher, C. (2011). A comparison of the Hadley circulation in modern reanalyses. *Journal of Geophysical Research*, *116*(D22), D22102. https://doi.org/10.1029/2011JD016677

Staten, P. W., Grise, K. M., Davis, S. M., Karnauskas, K., & Davis, N. (2019). Regional widening of tropical overturning: Forced change, natural variability, and recent trends. *Journal of Geophysical Research: Atmospheres*, *124*(12), 6104–6119. https://doi.org/10.1029/2018jd030100

Staten, P. W., Lu, J., Grise, K. M., Davis, S. M., & Birner, T. (2018). Re-examining tropical expansion. *Nature Climate Change*, *8*(9), 768–775. https://doi.org/10.1038/s41558-018-0246-2

Studholme, J., & Gulev, S. (2018). Concurrent changes to Hadley circulation and the meridional distribution of tropical cyclones. *Journal of Climate*, *31*(11), 4367–4389. https://doi.org/10.1175/JCLI-D-17-0852.1

Sun, Y., Li, L. Z. X., Ramstein, G., Zhou, T., Tan, N., Kageyama, M., & Wang, S. (2018). Regional meridional cells governing the interannual variability of the Hadley circulation in boreal winter. *Climate Dynamics*, *52*(1–2), 831–853. https://doi.org/10.1007/s00382-018-4263-7

Sun, Y., & Zhou, T. (2014). How does El Niño affect the interannual variability of the boreal summer Hadley circulation? *Journal of Climate*, *27*(7), 2622–2642. https://doi.org/10.1175/jcli-d-13-00277.1

Tao, L., Hu, Y., & Liu, J. (2015). Anthropogenic forcing on the Hadley circulation in CMIP5 simulations. *Climate Dynamics*, *46*(9–10), 3337–3350. https://doi.org/10.1007/s00382-015-2772-1

Trenberth, K. E., Stepaniak, D. P., & Caron, J. M. (2000). The global monsoon as seen through the divergent atmospheric circulation. *Journal of Climate*, *13*(22), 3969–3993. https://doi.org/10.1175/1520-0442(2000)013<3969:TGMAST>2.0.CO;2

Vera, C., Higgins, W., Amador, J., Ambrizzi, T., Garreaud, R., Gochis, D., et al. (2006). Toward a unified view of the American monsoon systems. *Journal of Climate*, *19*(20), 4977–5000. https://doi.org/10.1175/jcli3896.1

Wang, C., Hu, Y., Wen, X., Zhou, C., & Liu, J. (2020). Inter-model spread of the climatological annual mean Hadley circulation and its relationship with the double ITCZ bias in CMIP5. *Climate Dynamics*, *55*(9–10), 2823–2834. https://doi.org/10.1007/s00382-020-05414-z

Waugh, D. W., Garfinkel, C. I., & Polvani, L. M. (2015). Drivers of the recent tropical expansion in the Southern Hemisphere: Changing SSTs or ozone depletion? *Journal of Climate*, *28*(16), 6581–6586. https://doi.org/10.1175/JCLI-D-15-0138.1

Zhang, C. (1993). Large-scale variability of atmospheric deep convection in relation to sea-surface temperature in the tropics. *Journal of Climate*, *6*(10), 1898–1913. https://doi.org/10.1175/1520-0442(1993)006<1898:lsvoad>2.0.co;2

Zhang, C., Nolan, D. S., Thorncroft, C. D., & Nguyen, H. (2008). Shallow meridional circulations in the tropical atmosphere. *Journal of Climate*, *21*(14), 3453–3470. https://doi.org/10.1175/2007jcli1870.1

Zhang, G., & Wang, Z. (2013). Interannual variability of the Atlantic Hadley circulation in boreal summer and its impacts on tropical cyclone activity. *Journal of Climate*, *26*(21), 8529–8544. https://doi.org/10.1175/jcli-d-12-00802.1

Zhang, G., & Wang, Z. (2015). Interannual variability of tropical cyclone activity and regional Hadley circulation over the northeastern Pacific. *Geophysical Research Letters*, *42*(7), 2473–2481. https://doi.org/10.1002/2015GL063318

Zheng, F., Li, J., Wang, L., Xie, F., & Li, X. (2015). Cross-seasonal influence of the December–February Southern Hemisphere annular mode on March–May meridional circulation and precipitation. *Journal of Climate*, *28*(17), 6859–6881. https://doi.org/10.1175/jcli-d-14-00515.1